COMMUNICATIONS IN COMPUTATIONAL PHYSICS
Vol. **1**, No. 1, pp. 1-31

Commun. Comput. Phys.
February 2006

Two-Dimensional Multi-Domain Hybrid Spectral-WENO Methods for Conservation Laws

Bruno Costa[1], Wai Sun Don[2,*], David Gottlieb[2], Radislav Sendersky[2]

[1] *Departamento de Matemática Aplicada, IM-UFRJ, Caixa Postal 68530, Rio de Janeiro, RJ, C.E.P. 21945-970, Brazil.*
[2] *Division of Applied Mathematics, Brown University, Providence, Rhode Island 02912.*

Abstract. The multi-domain hybrid Spectral-WENO method (Hybrid) is introduced for the numerical solution of two dimensional nonlinear hyperbolic systems in a Cartesian physical domain which is partitioned into a grid of rectangular subdomains. The main idea of the Hybrid scheme is to conjugate the spectral and WENO methods for solving problems with shock or high gradients such that the scheme adapts its solver spatially and temporally depending on the smoothness of the solution in a given subdomain. Built as a multi-domain method, an adaptive algorithm is used to keep the solutions parts exhibiting high gradients and discontinuities always inside WENO subdomains while the smooth parts of the solution are kept inside a spectral one, avoiding oscillations related to the well-known Gibbs phenomenon and increasing the numerical efficiency of the overall scheme. A higher order version of the multiresolution analysis proposed by Harten is used to determine the smoothness of the solution in each subdomain. We also discuss interface conditions for the two dimensional problem and the switching procedure between WENO and spectral subdomains. The Hybrid method is applied to the two-dimensional Shock-Vortex Interaction and the Richtmyer-Meshkov Instability (RMI) problems.

Key words: Spectral, WENO, Multi-resolution, Multi-Domain, Hybrid, Conservation Laws

1 Introduction

In this article we extend the one-dimensional Multi-Domain Hybrid Spectral-WENO Method (Hybrid) for Hyperbolic Conservation Laws [6] to two-dimensions in space and apply it to the classical Shock-Vortex interaction and Richtmyer-Meshkov instabilities problem. The general idea of the Hybrid method is to use a multi-domain framework in order to apply convenient spatial discretizations to the smooth and rough parts of the numerical solution. Shocks and

---

[*] Correspondence to: Division of Applied Mathematics, Brown University, Providence, Rhode Island 02912. E-Mail: wsdon@dam.brown.edu

Report Documentation Page

Form Approved
OMB No. 0704-0188

1. REPORT DATE **2005**	2. REPORT TYPE	3. DATES COVERED **00-00-2005 to 00-00-2005**

4. TITLE AND SUBTITLE **Two-Dimensional Multi-Domain Hybrid Spectral-WENO Methods for Conservation Laws**	5a. CONTRACT NUMBER 5b. GRANT NUMBER 5c. PROGRAM ELEMENT NUMBER
6. AUTHOR(S)	5d. PROJECT NUMBER 5e. TASK NUMBER 5f. WORK UNIT NUMBER
7. PERFORMING ORGANIZATION NAME(S) AND ADDRESS(ES) **Brown University,Division of Applied Mathematics,182 George Street,Providence,RI,02912**	8. PERFORMING ORGANIZATION REPORT NUMBER
9. SPONSORING/MONITORING AGENCY NAME(S) AND ADDRESS(ES)	10. SPONSOR/MONITOR’S ACRONYM(S) 11. SPONSOR/MONITOR’S REPORT NUMBER(S)

12. DISTRIBUTION/AVAILABILITY STATEMENT
Approved for public release; distribution unlimited

13. SUPPLEMENTARY NOTES
The original document contains color images.

14. ABSTRACT

15. SUBJECT TERMS

16. SECURITY CLASSIFICATION OF:			17. LIMITATION OF ABSTRACT	18. NUMBER OF PAGES	19a. NAME OF RESPONSIBLE PERSON
a. REPORT **unclassified**	b. ABSTRACT **unclassified**	c. THIS PAGE **unclassified**		**31**	

Standard Form 298 (Rev. 8-98)
Prescribed by ANSI Std Z39-18

high gradients are kept at WENO subdomains, while complex, but still smooth, details of the solution are treated within spectral subdomains. Numerical efficiency is increased with respect to the classical spectral and WENO methods: Postprocessing techniques of the spectral method approach of shocks [11, 16] are avoided, since no Gibbs phenomenon will occur, and the expensive characteristic decompositions and projections of the WENO method are skipped at the smooth parts of the solution [2, 3, 5, 9, 10, 15].

The main issues in the construction of the Hybrid method are the smoothness measurement of the solution and the subdomains types switching algorithm. In this work we employ the high order multi-resolution algorithm by Ami Harten [12] to build a local classification of the solution into smooth and rough. Originally built to decrease the work of the fluxes computations of Conservation Laws, Harten's Algorithm proposes to use information from coarser grids when the solution is locally over-represented. We instead use the multi-resolution information to apply distinct numerical methodologies to the different structures of the solution. The main goal is to conjugate the higher efficiency of the spectral method with the shock-capturing capability of the WENO method. The multi-resolution analysis is used to trigger the switching algorithm to change the subdomains spatial discretizations if shocks start to develop at a spectral subdomain, or if the solution becomes smooth at a WENO one. Moving discontinuities are similarly treated by changing to (or maintaining as) WENO the subdomains on their paths and switching to (or maintaining as) spectral the subdomains that were left behind. These changes are performed via Lagrangian and spectral interpolations of the local solutions to the new discretizations grids. Interpolation is also used to patch the solutions at the interfaces. While a simple average is sufficient for the interfaces where the solution is smooth, using the same grid spacing at adjacent WENO subdomains is necessary for a conservative transmission of shocks [24]. Even though we do not have a theoretical proof of the conservation of the Hybrid scheme, we argue that with the conjugation of two conservative schemes with a conservative WENO interface and the high order accuracy of the conservative spectral scheme, the conservation error should be spectrally small. We have numerically demonstrated this fact in [6] through a long time integration of the inviscid Burgers equations with correct shock speed and achieved excellent agreement with the analytical solution of the standard Riemann shock-tube problems, such as the Lax and the Sod problem of the Euler Equations.

The paper is organized as follows: Section 2 provides quick reviews on spectral and WENO methods. The Multi-Resolution analysis is discussed in details at Section 3 and the Hybrid Method is introduced at Section 4. The Switching Algorithm is presented in Section 4.3 and numerical experiments with two dimensional compressible flows are finally presented at Section 5. Concluding remarks are given in Section 6.

2 Spectral and WENO Methods

2.1 The Spectral Method

In spectral collocation methods, the function $u(x)$ is interpolated by a global Lagrangian interpolation polynomial of degree $N, l_j(x)$, at a given set of collocation points $\{x_j, j = 0, \ldots, N\}$

as

$$I_N u(x) = \sum_{j=0}^{N} u(x_j) l_j(x) \quad , \tag{2.1}$$

where I_N is the Interpolating operator and $l_j(x_i) = \delta_{ij}$.

The Lagrangian interpolation polynomial $l_j(x)$ can be constructed as

$$l_j(x) = \frac{q(x)}{(x - x_j) q'(x_j)}, \qquad q(x) = \prod_{j=0}^{N} (x - x_j) \tag{2.2}$$

and the derivative of $I_N u$ becomes

$$\frac{d I_N u(x)}{dx} = \sum_{j=0}^{N} u(x_j) \frac{d l_j(x)}{dx} \quad . \tag{2.3}$$

In this study, we will employ the Chebyshev-Gauss-Lobatto quadrature points, namely,

$$x_j = \cos\left(\frac{\pi j}{N}\right) \quad , \tag{2.4}$$

which are the roots of $(1 - x^2) T'_N(x)$ and $T_N(x)$ is the N_th degree Chebyshev polynomial of the first kind. The Chebyshev interpolation polynomial is given by

$$l_j(x) = \frac{(-1)^{j+1} (1 - x^2) T'_N(x)}{c_j N^2 (x - x_j)} \quad . \tag{2.5}$$

where $c_j = 1, j = 1, \ldots, N - 1$ and $c_0 = c_N = 2$.

The form of the differentiation matrix $\mathbf{D} = \frac{dl_j(x_i)}{dx}$ in (2.3) can be found in [7]. The mapping devised by Kosloff and Tal-Ezer [18] will also be employed to enhance the stability of the Chebyshev collocation scheme [4, 8].

2.2 Filters

Spectral methods are highly efficient and accurate, when the solution and its derivatives are smooth. In the presence of discontinuities, however, Gibbs Phenomenon generates oscillations that contaminate the solution and causes the loss of the exponential convergence. This is explained in spectral space by the linear decay rate of the coefficients a_n of the global expansion:

$$u(x) = \sum_{n=0}^{\infty} a_n T_n(x). \tag{2.6}$$

In such a situation, one can modify the global expansion coefficients a_n to enhance the convergence properties of the approximation via a filter function $\sigma(\eta)$ [26] with the following properties

$$\begin{aligned} \sigma(\eta) &= \sigma(-\eta), \quad \sigma(\pm 1) = 0 \quad , \\ \sigma(0) &= 1, \quad \sigma^{(q)}(0) = 0 \quad q = 1, \ldots, p - 1 \quad . \end{aligned} \tag{2.7}$$

If $\sigma(\eta)$ has at least $p-1$ continuous derivatives, $\sigma(\eta)$ is termed a p_th order filter. It was proved in [26] that the filtered expansion converges faster to the correct solution than the unfiltered original one in the case of a discontinuous function. Moreover, the convergence rate depends solely on the order and the compactness of the filter function $\sigma(\eta)$ and the distance from the discontinuities.

The filter function used in this study is the Exponential filter given by

$$\sigma(\eta) = \exp(-\alpha\eta^p) \quad , \tag{2.8}$$

where $\alpha = -\ln(\epsilon)$ and ϵ is the machine zero.

The spectral filtering can be expressed

- in the physical space as:

$$F_N u(x_i) = \sum_{j=0}^{N} u(x_j)\Phi_{ji}, \quad \Phi_{ji} = \frac{2}{Nc_j}\sum_{n=0}^{N}\frac{1}{c_n}\sigma\left(\frac{n}{N}\right)T_n(x_i)T_n(x_j) \quad , \tag{2.9}$$

- in the transformed space as:

$$F_N u(x_i) = \sum_{n=0}^{N} a_n\sigma\left(\frac{n}{N}\right)T_n(x_i), \quad a_n = \frac{2}{Nc_n}\sum_{j=0}^{N}\frac{1}{c_j}u_jT_n(x_j) \quad , \tag{2.10}$$

where F_N is the filtering operator.

While filtering techniques can improve the overall convergence properties of the solution away from discontinuities, the solution near the discontinuities remains poor. Post-processing of the resulting oscillatory data to recover spectrally accurate non-oscillatory results can be performed by various reconstruction techniques, such as the direct and inverse Gegenbauer reconstruction [11, 16] and Padé reconstruction [21]. Reconstruction techniques are, in general, computationally costly and certain complications might arise. For instance, as the degree of the reconstructed polynomial increases, the Gegenbauer transformation matrices become ill-conditioned due to the round-off error [16]. Moreover, the extension of these reconstruction techniques to higher dimensions is not trivial.

2.3 The WENO Method

WENO schemes were designed for the numerical solution of Hyperbolic Conservation Laws in the form (for ease of presentation the discussion is based on the one-dimensional formulation)

$$\mathbf{u}_t + \mathbf{f}(\mathbf{u})_x = 0 \quad . \tag{2.11}$$

The Jacobian $\frac{\partial \mathbf{f}}{\partial \mathbf{u}}$ for (2.11) is needed to project the system into its characteristic form and, in general, $\frac{\partial \mathbf{f}}{\partial \mathbf{u}}$ is not constant. To overcome the difficulty when computing the flux at a cell boundary $x_{i+\frac{1}{2}}$, "local freezing" of the matrix components is employed using the Roe average $\mathbf{u}_{i+\frac{1}{2}}$ [23] defined as

$$f(\mathbf{u}_{i+1}) - f(\mathbf{u}_i) = f'(\mathbf{u}_{i+\frac{1}{2}})(\mathbf{u}_{i+1} - \mathbf{u}_i) \quad . \tag{2.12}$$

The numerical scheme for (2.11) can be written in the conservative form as

$$\frac{du_i(t)}{dt} = -\frac{1}{\Delta x}(\hat{f}_{i+\frac{1}{2}} - \hat{f}_{i-\frac{1}{2}}) \quad , \tag{2.13}$$

where $u_i(t)$ is the numerical approximation to the point value $u(x_i, t)$ and Δx is the uniform grid spacing. The numerical flux based on the $\{u_j, j = i - r, \ldots, i + s\}$

$$\hat{f}_{i+\frac{1}{2}} = \hat{f}(u_{i-r}, \ldots, u_{i+s}) \quad , \tag{2.14}$$

satisfies the following conditions:

- $\hat{f}$ is Lipschitz continuous in all arguments;
- $\hat{f}$ is consistent with the physical flux f, i.e. $\hat{f}(u, \ldots, u) = f(u)$.

The solution to the conservative scheme (2.13), if converges, will converge to a weak solution. This is known as the Lax-Wendroff theorem.

The earlier works of van Leer [25], Boris and Book [1] and Harten's TVD schemes have led to the introduction of Essentially Non-Oscillatory (ENO) schemes [14], where its basic premise is that of adaptivity of the stencil, based on the local smoothness of the solution, using only a stencil free of discontinuities in the computation of flux gradients. ENO schemes have been shown to generate sharp resolutions of shocks as well as to maintain high order of accuracy in smooth regions.

An improvement of finite volume ENO – Weighted Essentially Non-Oscillatory (WENO) schemes were proposed by Liu, Osher, and Chan [19]. WENO schemes use the same idea as ENO, except that WENO uses a convex combination of all available smooth stencils to obtain higher order of accuracy than the original ENO at smooth parts of the solution. Finite Difference WENO schemes were later proposed by Jiang and Shu [15].

In all numerical examples that follows, we use the fifth order characteristic-wise WENO finite difference formulation, making use of the Roe average for the eigensystem defined above and the global Lax-Fredrichs flux splitting

$$f^{\pm} = \frac{1}{2}(f(u) \pm \alpha u) \quad , \tag{2.15}$$

where $\alpha = \max_u \max_{1 \leq i \leq N_\lambda} |\lambda_i(u)|$ and $\lambda_i(u), i = 1, \ldots, N_\lambda$ are the local eigenvalues of the Jacobian $\frac{\partial \mathbf{f}}{\partial \mathbf{u}}$. The numerical flux $\hat{f}_{i+\frac{1}{2}}$ is computed by the WENO reconstruction procedure. The interested reader is referred to [3] for details.

3 Multi-Resolution Analysis

The successful implementation of the Hybrid method depends on the ability to obtain accurate information on the smoothness of a function. In this work, we employ the Multi-Resolution (MR) algorithms by Harten [12, 13] to detect the smooth and rough parts of the numerical solution. The general idea is to generate a coarser grid of averages of the point values of a function and measure the differences (MR coefficients) d_i between the interpolated values from this sub-grid and the point values themselves. A tolerance parameter ϵ_{MR} is chosen in order to classify as smooth those parts of the function that can be well interpolated by the averaged function and as rough those where the differences d_i are larger than the parameter ϵ_{MR}. We shall see that the order of interpolation is relevant and the ratio between d_i of distinct orders may also be taken as an indication of smoothness.

Let us start by showing two examples where one can notice the detection capabilities of the Multi-Resolution analysis that will be presented below. The left and right figures of Figure 1 show the piecewise analytic function

$$f(x) = \begin{cases} 10 + x^3 & -1 \le x < -0.5 \\ x^3 & -0.5 \le x < 0 \\ \sin(2\pi x) & 0 \le x \le 1 \end{cases}, \tag{3.1}$$

and the density (ρ) of the Mach 3 Shock-Entropy wave interaction problem [15] as computed by the classical fifth order WENO finite difference scheme, respectively.

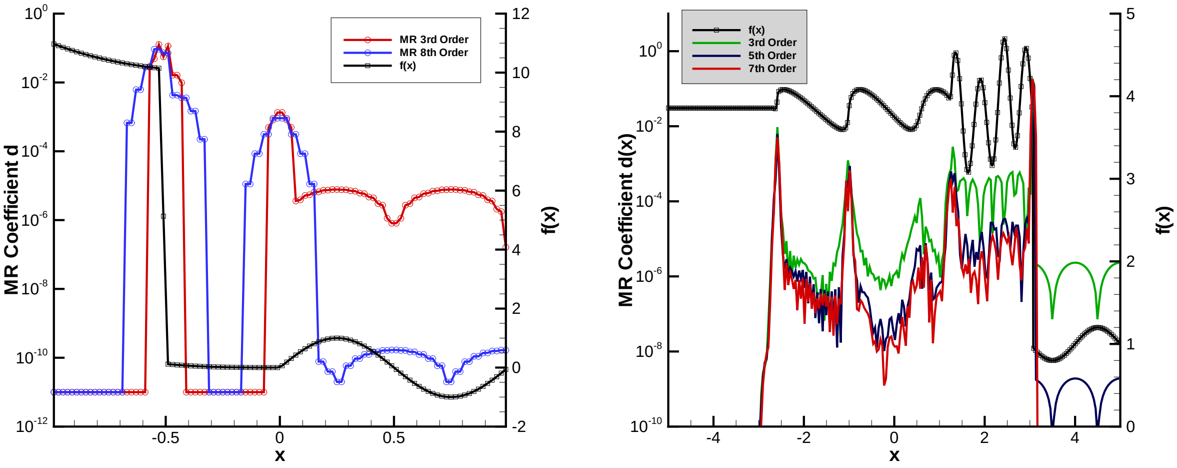

Figure 1: (Left) The third and eighth order MR coefficients d_i of the piecewise analytic function. (Right) The third, fifth and seventh order MR coefficients d_i of the density $f(x) = \rho$ of the Mach 3 Shock-Entropy wave interaction problem.

The test function (3.1) has a jump discontinuity at $x = -0.5$ and a discontinuity at its first derivative at $x = 0$. One can see that at each grid point the differences d_i decay exponentially to zero inside the analytical pieces of the function when the order of interpolation increases from $n_{MR} = 3$ to $n_{MR} = 8$. At the discontinuity $x = 0.5$, the measured differences d_i are $O(1)$ and remain unchanged despite the increase of the interpolation order. Similar behavior is exhibited at the derivative discontinuity at $x = 0$ with a smaller amplitude.

Also, in the right figure of Figure 1, the density of the Mach 3 Shock-Entropy wave interaction problem and the corresponding MR coefficients d_i are shown for the third, fifth and seventh order Multi-Resolution analysis. The location of the main shock is at $x \approx 2.73$ and the shocklets behind the main shock are well captured. The high frequencies behind the main shock are much better distinguished with the higher orders.

Averaging a function corresponds to filter the upper half of the spectrum. The main idea of Hartens smoothness classification is to measure how distant the actual values of the function are from being predicted through interpolation of the lower half of the frequencies contained in the sub-grid of averages. We now describe a detailed construction of the sub-grid of averages and its corresponding interpolating polynomial, finishing with a worked example.

Given an initial number of grid points N_0 and grid spacing Δx_0, consider the set of nested dyadic grids $\{G^k, 0 \leq k \leq L\}$, defined as:

$$G^k = \{x_i^k, i = 0, \dots, N_k\}, \tag{3.2}$$

where $x_i^k = i\Delta x_k, \Delta x_k = 2^k \Delta x_0, N_k = 2^{-k} N_0$. For each level $k > 0$ we define the set of cell averages $\{\bar{f}_i^k, i = 1, \dots, N_k\}$ at x_i^k of a function $f(x)$:

$$\bar{f}_i^k = \frac{1}{\Delta x_k} \int_{x_{i-1}^k}^{x_i^k} f(x) dx, \tag{3.3}$$

and $\bar{f}_i^0 = f_i^0$. Let $\tilde{f}_{2i-1}^k$ be the approximation to $\bar{f}_{2i-1}^k$ by the unique polynomial of degree $2s$ that interpolates $\bar{f}_{i+l}^k, |l| \leq s$ at x_{i+l}^k, where $r = 2s + 1$ is the order of approximation.

The approximation differences, also called multiresolution coefficients, $d_i^k = \bar{f}_{2i-1}^{k-1} - \tilde{f}_{2i-1}^{k-1}$, at the k_th grid level and grid point x_i, have the property that if $f(x)$ has $p - 1$ continuous derivatives and a jump discontinuity at its p_th derivative, then

$$d_i^k \approx \begin{cases} \Delta x_k^p [f_i^{(p)}] & \text{for} \quad p \leq r \\ \Delta x_k^r f_i^{(r)} & \text{for} \quad p > r \end{cases}, \tag{3.4}$$

where $[\cdot]$ denotes the magnitude of the jump of the function inside.

From formula (3.4) it follows that

$$|d_{2i}^{k-1}| \approx 2^{-\bar{p}} |d_i^k|, \qquad \text{where} \qquad \bar{p} = \min\{p, r\}. \tag{3.5}$$

Equation (3.5) shows that away from discontinuities, the MR coefficients d_i^k diminish in size with the refinement of the grid; close to discontinuities, they remain the same size, independent of k. The MR coefficients d_i^k were used in [13] in two ways. First, finer grid data $\bar{f}_i^0$ were mapped to its M level multiresolution representation $\bar{f}_i^0 = (d_i^1, \cdots, d_i^M, \bar{f}_i^M)$ to form a multiscale version of a particular scheme, where truncation of small quantities with respect to a tolerance parameter decreased the number of flux computations. Secondly, the MR coefficients d_i^k also acted as a shock detection mechanism and an adaptive method was designed where a second-order Lax-Wendroff scheme was locally switched to a first-order accurate TVD Roe scheme, whenever d_i^1 was bigger than ϵ_{MR}.

Equation (3.4) also indicates that the variation of the MR order, n_{MR}, can give additional information on the type of the discontinuity. Nevertheless, in this work, we will be limited at using only the first level $k = 1$ of the multiresolution coefficients and we shall drop the superscript 1 from the d_i^1 from here on unless noted otherwise.

Hence, to find d_i, the idea is to construct a piecewise polynomial $P_k(x)$ of degree $k = n_{MR}$ using $k+1$ computed average values of f_i, $\bar{f}_i$, at the equi-spaced grid x_i such that

$$P_k(x_i) = f(x_i) + O(\Delta x^{k+1}), \tag{3.6}$$

and

$$d_i = f_i - P_k(x_i). \tag{3.7}$$

Given a tolerance level ϵ_{MR}, the smoothness of the function $f(x)$ at x_i would then be checked against the magnitude of the d_i, namely:

$$\begin{cases} |d_i| \leq \epsilon_{MR} & \Rightarrow \text{solution is smooth.} \\ |d_i| > \epsilon_{MR} & \Rightarrow \text{solution is non-smooth.} \end{cases} \tag{3.8}$$

The algorithm for computing the MR coefficients d_i is given next.

3.1 Computing the MR Coefficients

Consider an equi-spaced grid $\{x_i = i\Delta x, i = -m, \ldots, 0, \ldots, N, \ldots, N+M\}$ where Δx is the constant grid spacing. N can be an odd or an even number. Depending on N and the even or odd order of the MR Analysis n_{MR}, the number of ghost points m and M required are given in table I.

N	n_{MR}	m	M
odd	odd	$n_{MR}+1$	$n_{MR}+1$
even	odd	$n_{MR}+1$	n_{MR}
odd	even	n_{MR}	$n_{MR}+2$
even	even	n_{MR}	$n_{MR}+1$

Table I: The number of ghost points m and M required for the MR Analysis.

Given the grid point values of the function $f(x)$, the average values are computed as

$$\bar{f}_i = \frac{1}{2}\left(f_{2i} + f_{2i+1}\right), \quad i = -\frac{m}{2}, \ldots, \frac{N+M-1}{2}. \tag{3.9}$$

We construct a piecewise $k = n_{MR}$ degree polynomial $P_k(x)$ using the $k+1$ computed average values of the given function, $\bar{f}_i$ such that

$$P_k(x_i) = f(x_i) + O(\Delta x^{k+1}). \tag{3.10}$$

The polynomial $P_k(x_i)$, $l = \frac{1}{2}m$ and $L = l-1$ or $L = l$ if k is odd or even, respectively, can be written as

$$P_k(x_i) = \sum_{r=i-l}^{i+L} \alpha_r \bar{f}_r. \tag{3.11}$$

However, since the coefficients α depend only on x_i and do not depend on the function $f(x)$, the $P_k(x_i)$ can be written as:

$$P_k(x_i) = \begin{cases} \sum_{r=-l}^{L} \alpha_r \bar{f}_{i+r}, & \mathrm{mod}(i,2) = 0 \\ \sum_{r=-l}^{L} \beta_{r+1} \bar{f}_{i+r}, & \mathrm{mod}(i,2) = 1 \end{cases}. \tag{3.12}$$

In the case of $\mathrm{mod}(i,2) = 1$,

$$\beta_{-r} = \alpha_r, \quad r = -l, \ldots, L. \tag{3.13}$$

Furthermore, if n_{MR} is even, the coefficients α are symmetric about $r = 0$, namely, $\alpha_{-r} = \alpha_r, r = 1, \ldots, L$.

The desired coefficients α are computed by requiring $P_k(x)$ to be equal to each of the first $k+1$ monomials $f(x) = 1, x, x^2, \ldots, x^k$ and evaluated at any grid point $x = x^*$. For simplicity, we take $x^* = 0$. The $\bar{f}_i$ are evaluated for $i = -l, \ldots, L$. This procedure results in a system of linear equations, $\mathbf{A}\vec{\alpha} = \vec{b}$, where

$$\mathbf{A} = \begin{pmatrix} 1 & \ldots & 1 \\ -2l + (-2l+1) & \ldots & 2L + (2L+1) \\ \vdots & \vdots & \vdots \\ (-2l)^k + (-2l+1)^k & \ldots & (2L)^k + (2L+1)^k \end{pmatrix}, \overrightarrow{\alpha} = \begin{pmatrix} \alpha_{-l} \\ \alpha_{-l+1} \\ \vdots \\ \alpha_L \end{pmatrix}, \overrightarrow{b} = \begin{pmatrix} 1 \\ 0 \\ \vdots \\ 0 \end{pmatrix}, \tag{3.14}$$

and $\mathbf{A}$ is a matrix of size $(L+l+1) \times (L+l+1)$.

Using (3.12), the k-th order Multi-Resolution coefficients d_i at x_i can be computed as

$$d_i = f_i - P_k(x_i) \quad i = 0, \ldots, N. \tag{3.15}$$

One can also evaluate the α by matching the terms in the Taylor series expansion using (3.10) and (3.11) to any desired order, however this procedure may become cumbersome for high order k.

Example

To illustrate the procedure above, we will construct two unique local polynomials with $k = n_{MR} = 3$, such that $P_k(x_0) = f(x_0) + O(\Delta x^{k+1})$ and $P_k(x_1) = f(x_1) + O(\Delta x^{k+1})$.

To construct the desired polynomials one needs to find the unique coefficients $\{\alpha_{-2}, \alpha_{-1}, \alpha_0, \alpha_1\}$ and $\{\beta_{-1}, \beta_0, \beta_1, \beta_2\}$ such that

$$\alpha_{-2}\bar{f}_{-2} + \alpha_{-1}\bar{f}_{-1} + \alpha_0\bar{f}_0 + \alpha_1\bar{f}_1 = f(x_0) + O(\Delta x^4) \tag{3.16}$$

and

$$\beta_{-1}\bar{f}_{-1} + \beta_0\bar{f}_0 + \beta_1\bar{f}_1 + \beta_2\bar{f}_2 = f(x_1) + O(\Delta x^4). \tag{3.17}$$

The system of equations, (3.14), becomes

$$\mathbf{A} = \begin{pmatrix} 1 & 1 & 1 & 1 \\ -7 & -3 & 1 & 5 \\ 25 & 5 & 1 & 13 \\ -91 & -9 & 1 & 35 \end{pmatrix}, \quad \overrightarrow{\alpha} = \begin{pmatrix} \alpha_{-2} \\ \alpha_{-1} \\ \alpha_0 \\ \alpha_1 \end{pmatrix}, \quad \overrightarrow{b} = \begin{pmatrix} 1 \\ 0 \\ 0 \\ 0 \end{pmatrix}. \tag{3.18}$$

Solving this system yields

$$\alpha_{-2} = -\frac{3}{64}, \quad \alpha_{-1} = \frac{17}{64}, \quad \alpha_0 = \frac{55}{64}, \quad \alpha_1 = -\frac{5}{64}, \tag{3.19}$$

and $\{\beta_{-1} = \alpha_1, \beta_0 = \alpha_0, \beta_1 = \alpha_{-1}, \beta_2 = \alpha_{-2}\}$.

Remark 3.1. The tolerance parameter ϵ_{MR} determines the dynamic activation of the spectral and WENO spatial discretizations along the various subdomains of the hybrid method. While a too small value of ϵ_{MR} activates the more expensive WENO method at subdomains where the solution is smooth, a larger value activates the spectral method at a subdomain with low spatial resolution, generating oscillations. ϵ_{MR} also bears a straight relation with the interpolation order n_{MR}. High n_{MR} values decrease the size of ϵ_{MR} one needs to chose, since high frequencies are less mistaken by gradient jumps. The general guideline is to start with a value for n_{MR} at least equal to the order of the WENO method and increase it according to the complexity of the solution. For instance, $n_{MR} = 5$ is a good choice for the piecewise smooth solution of the SOD problem, the Entropy problem would work better with $n_{MR} = 7$. For most of the flows with shock that were tested, the value of $\epsilon_{MR} = 10^{-3}$ yielded a good balance between computational speed and accuracy of the numerical solution.

4 The Multi-Domain Hybrid Spectral-WENO method

We now describe the implementation of the Multi-Domain Hybrid Spectral-WENO method (Hybrid), detailing the structure of the two-dimensional grid of subdomains, the interfaces treatment and the algorithm that switches the spatial discretization of the subdomains.

The main idea of the Hybrid method can be formulated as:
Avoid Gibbs phenomenon by keeping discontinuities at WENO subdomains and increase the numerical efficiency by treating the smooth parts of the solution using a spectral spatial discretization.

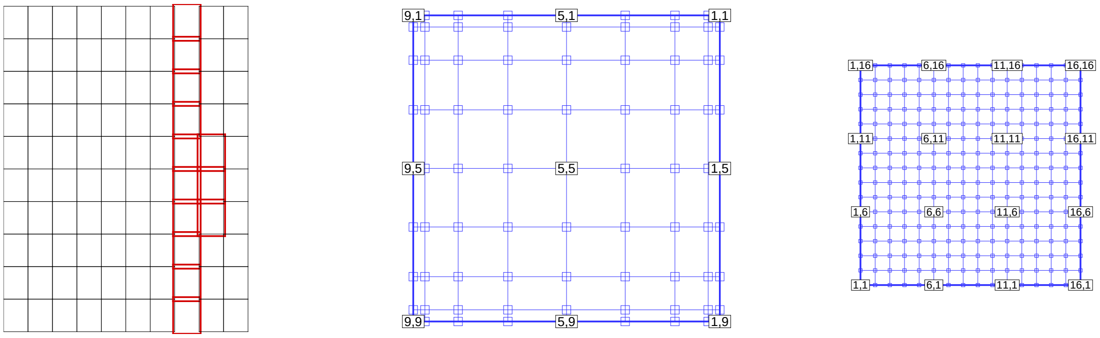

Figure 2: (Left) Partition of the physical domain into spectral and WENO subdomains. (Middle) Typical spectral subdomain. (Right) Typical WENO subdomain.

In this study, the physical domain is restricted to rectangular shapes and will be partitioned into a $(N_d^x \times N_d^y)$ grid of subdomains. Figure 2 shows an example of such a domain partition along with typical spectral and WENO subdomains. Note that patching of subdomains occurs due to the ghost points of the WENO discretization.

We shall use a vector $\mathbf{k} = (k_x, k_y), k_x = 1, \ldots, N_d^x, k_y = 1, \ldots, N_d^y$ to denote the coordinates of the two dimensional subdomain grid. For example, $\mathbf{k} = (2, 3)$ means the subdomain number $k_x = 2$ in the x direction and $k_y = 3$ in the y direction. Each subdomain is initialized either as a spectral or WENO subdomain. The Chebyshev-Gauss-Lobatto points are used for the spectral discretization and an uniformly spaced grid with ghost points is used as the WENO grid.

For the sake of simplicity, we consider only square subdomains, with $N_S \times N_S$ grid points at a pectral subdomain and $N_W \times N_W$ equi-spaced points at a WENO subdomain. The number of ghost points is denoted by r and N_B is the number of points used for the buffer zone (see below).

4.1 Description of WENO subdomains

Each WENO subdomain $\mathbf{k}$ is composed of three parts: The "Ghost Area", the "Buffer Area", and the "Interior Area" as shown in Figure 3.

- **Ghost Area:**
  The "Ghost Area" is used for the WENO Reconstruction and for communication with its neighboring subdomains and is subdivided into eight "Ghost Zones" $\{G_i^{\mathbf{k}}, \quad i = 1, \ldots, 8\}$ (see the middle figure of Figure 3),

$$\left\{ \begin{array}{ccccc} G_8^{\mathbf{k}} = I_0^g \times J_2^g & , & G_7^{\mathbf{k}} = I_1^g \times J_2^g & , & G_6^{\mathbf{k}} = I_2^g \times J_2^g \\ G_1^{\mathbf{k}} = I_0^g \times J_1^g & , & & , & G_5^{\mathbf{k}} = I_2^g \times J_1^g \\ G_2^{\mathbf{k}} = I_0^g \times J_0^g & , & G_3^{\mathbf{k}} = I_1^g \times J_0^g & , & G_4^{\mathbf{k}} = I_2^g \times J_0^g \end{array} \right\} , \tag{4.1}$$

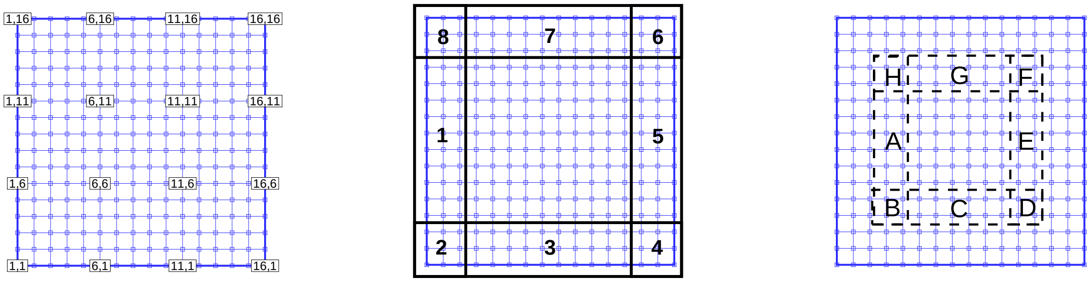

Figure 3: (Left) Typical WENO subdomain. (Middle) "Ghost Area". (Right) "Buffer Area".

where the stencil ranges are

$$\begin{aligned} I_0^g &= \{x_{-r},\ldots,x_{-1}\}, \quad I_1^g = \{x_0,\ldots,x_N\}, \quad I_2^g = \{x_{N+1},\ldots,x_{N+r}\}, \\ J_0^g &= \{y_{-r},\ldots,y_{-1}\}, \quad J_1^g = \{y_0,\ldots,y_N\}, \quad J_2^g = \{y_{N+1},\ldots,y_{N+r}\}, \end{aligned}$$

with $N = N_W$.

- **Buffer Area:**
  The Buffer Area is used for the treatment of moving discontinuities. If a high gradient or shock is detected inside a buffer zone, the closest neighboring spectral subdomain(s) is switched to WENO subdomain(s).

  For two-dimensional problems, each WENO subdomain has eight "Buffer Zones" $\{B_i^{\mathbf{k}}, \quad i = \mathbf{A},\ldots,\mathbf{H}\}$ (see the right figure of Figure 3),

$$\left\{ \begin{array}{lclcl} B_{\mathbf{H}}^{\mathbf{k}} = I_0^b \times J_2^b & , & B_{\mathbf{G}}^{\mathbf{k}} = I_1^b \times J_2^b & , & B_{\mathbf{F}}^{\mathbf{k}} = I_2^b \times J_2^b \\ B_{\mathbf{A}}^{\mathbf{k}} = I_0^b \times J_1^b & , & & , & B_{\mathbf{E}}^{\mathbf{k}} = I_2^b \times J_1^b \\ B_{\mathbf{B}}^{\mathbf{k}} = I_0^b \times J_0^b & , & B_{\mathbf{C}}^{\mathbf{k}} = I_1^b \times J_0^b & , & B_{\mathbf{D}}^{\mathbf{k}} = I_2^b \times J_0^b \end{array} \right\} , \tag{4.2}$$

  where the stencil ranges are given by

$$\begin{aligned} I_0^b &= \{x_0,\ldots,x_M\}, \quad I_1^b = \{x_{M+1},\ldots,x_{N-M}\}, \quad I_2^b = \{x_{N-M+1},\ldots,x_N\}, \\ J_0^b &= \{y_0,\ldots,y_M\}, \quad J_1^b = \{y_{M+1},\ldots,y_{N-M}\}, \quad J_2^b = \{y_{N-M+1},\ldots,y_N\}, \end{aligned}$$

  with $N = N_W$ and $M = N_B$. As greater is the value of N_B, earlier is the detection of shocks and gradients, however, at the cost of early switching of the neighboring subdomains to WENO and greater chance of unnecessary costly computations. Satisfactory results have been obtained with the default $M = r$ in this study. It should be noted that these buffer zone grid points are part of the interior grid points and should not be confused with WENO ghost points.

- **Interior Area:**
  Finally, the "Interior Area" is all the WENO grid points $W^{\mathbf{k}}$ excluding the "Ghost Area" and "Buffer Area", $I^{\mathbf{k}} = W^{\mathbf{k}}/(\bigcup_i G_i^{\mathbf{k}} \bigoplus \bigcup_i B_i^{\mathbf{k}})$. If the high gradient stays inside this area, no action is required by the neighbors.

4.2 Interface Conditions

The following configurations are representative of any two-dimensional domain partitions:

- Spectral-Spectral-Spectral-Spectral (Figure 4)
- Spectral-Spectral-Spectral-WENO (Figure 6)
- Spectral-Spectral-WENO-WENO (Figure 6)
- Spectral-WENO-WENO-WENO (Figure 6)
- WENO-WENO-WENO-WENO (Figure 5)

The functional values in the spectral and WENO subdomains are denoted by $s_{ij}^{\mathbf{k}}$ and $w_{ij}^{\mathbf{k}}$ respectively at (x_i, y_j) in the respective subdomain $\mathbf{k}$. Centered at the subdomain $\mathbf{k}$, we define the superscripts $\mathbf{k}_0, \mathbf{k}_1, \mathbf{k}_2, \mathbf{k}_3, \mathbf{k}_4, \mathbf{k}_5, \mathbf{k}_6, \mathbf{k}_7, \mathbf{k}_8$ as

$$\begin{pmatrix} \mathbf{k}_8 = \mathbf{k} + (-1,+1) & , & \mathbf{k}_7 = \mathbf{k} + (+0,+1) & , & \mathbf{k}_6 = \mathbf{k} + (+1,+1) \\ \mathbf{k}_1 = \mathbf{k} + (-1,+0) & , & \mathbf{k}_0 = \mathbf{k} & , & \mathbf{k}_5 = \mathbf{k} + (+1,+0) \\ \mathbf{k}_2 = \mathbf{k} + (-1,-1) & , & \mathbf{k}_3 = \mathbf{k} + (+0,-1) & , & \mathbf{k}_4 = \mathbf{k} + (+1,-1) \end{pmatrix} \quad , \tag{4.3}$$

and they denote the Center ($\mathbf{k}_0$), Left ($\mathbf{k}_1$), Bottom-Left ($\mathbf{k}_2$), Bottom ($\mathbf{k}_3$), Bottom-Right ($\mathbf{k}_4$), Right ($\mathbf{k}_5$), Top-Right ($\mathbf{k}_6$), Top ($\mathbf{k}_7$), and Top-Left($\mathbf{k}_8$) subdomains of subdomain $\mathbf{k} = \mathbf{k}_0$ respectively. For example $s_{ij}^{\mathbf{k}_1}$ is to be interpreted as a value at the point (x_i, y_j) in the spectral Left subdomain $\mathbf{k}_1 = \mathbf{k} + (-1, +0)$. The subdomain interfaces consist of corners and shared sides among the spectral and WENO subdomains.

Spectral-Spectral Interface

Corners only appear at the connection of two or more spectral subdomains, since the grid points of the WENO subdomains never coincide with the spectral collocation points at the interface. Corner values are assigned with the average of the values of all connecting subdomains. For example, in figure 4, assuming that S^1 is the reference subdomain $\mathbf{k}_0$ and $N = N_S$,

$$s_{0N}^{\mathbf{k}_0} = s_{00}^{\mathbf{k}_3} = s_{N0}^{\mathbf{k}_4} = s_{NN}^{\mathbf{k}_5} = \frac{1}{4}\left(s_{0N}^{\mathbf{k}_0} + s_{00}^{\mathbf{k}_3} + s_{N0}^{\mathbf{k}_4} + s_{NN}^{\mathbf{k}_5}\right) \quad . \tag{4.4}$$

Along the interface between two spectral subdomains, the values at the shared side are computed similarly by assigning the average of the two values of the connected subdomains at

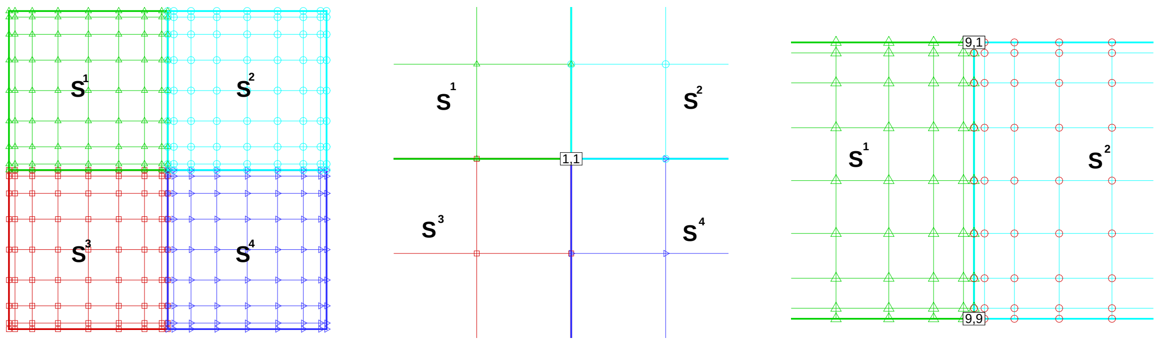

Figure 4: (Left) Spectral-Spectral-Spectral-Spectral subdomains configuration. (Middle) Corner point of all four spectral subdomains. (Right) Shared side of two spectral subdomains.

all collocation points. Consider the interface between the two spectral subdomains $S^1 - S^2$ (the rightmost figure of Figure 4),

$$s_{0j}^{\mathbf{k}_0} = s_{Nj}^{\mathbf{k}_5} = \frac{1}{2}\left(s_{0j}^{\mathbf{k}_0} + s_{Nj}^{\mathbf{k}_5}\right), \quad j = 0, \ldots, N \quad . \tag{4.5}$$

The other spectral subdomains' corners and sides are treated similarly.

Note 4.1. In case of adjacent subdomains with different numbers of collocation points, global interpolation can be used before averaging.

Note 4.2. An exact Riemannn solver and penalty interface conditions had been tried but no discernible differences were observed from the simple average.

WENO-WENO Interface

To maintain conservation, adjacent WENO subdomains are required to have the same spacing Δx (see [24]). This implies that ghost points of a WENO subdomain match the interior points of the neighboring WENO subdomain (see Figure 5). Thus, simple copying of the solution values of the neighboring interior points to the "Ghost Area" is sufficient for the communication of WENO subdomains.

For instance the middle figure of Figure 5 shows two "Ghost Zones": The zone in the solid rectangle corresponds to the "Ghost Zone" $G_5^{\mathbf{k}}$ of W^1; and the zone in the dash-dotted rectangle corresponds to the "Ghost Zone" $G_1^{\mathbf{k}}$ of W^2 (see 4.1). In this case, by denoting $N = N_W$ and using W^1 as a reference subdomain (subdomain $\mathbf{k} = \mathbf{k}_0$)

$$w_{(N+l)j}^{\mathbf{k}_0} = w_{lj}^{\mathbf{k}_5}, \quad w_{-lj}^{\mathbf{k}_5} = w_{(N+1-l)j}^{\mathbf{k}_0} \quad j = -r, \ldots, N+r, \quad l = 1, \ldots, r \quad , \tag{4.6}$$

where r is the number of ghost points.

Note 4.3. In general the number of "ghost" points in each subdomain does not have to be the same as long as the same grid spacing Δx is used at all the neighboring subdomains.

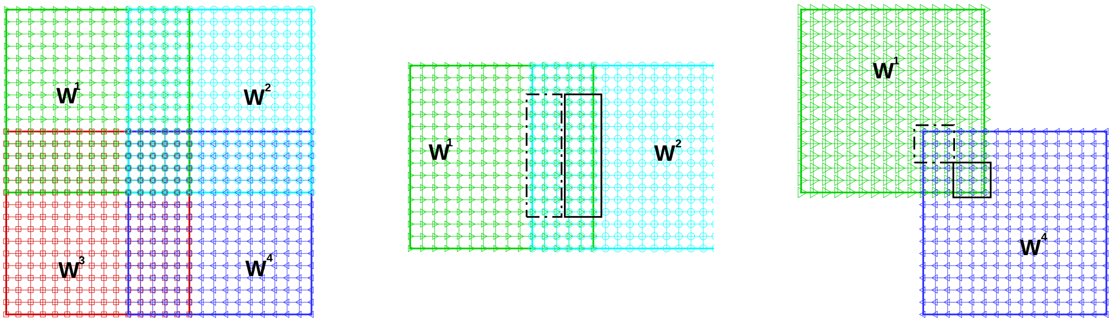

Figure 5: (Left) WENO-WENO-WENO-WENO subdomain configuration. (Middle) $W^1 - W^2$ Interface. (Right) $W^1 - W^4$ Interface.

Spectral-WENO Interface

Spectral-WENO interface can be found in the configurations shown in Figure 6.

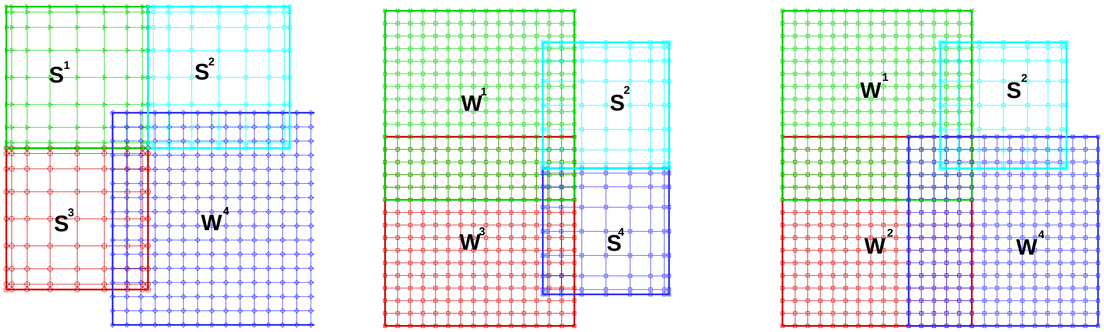

Figure 6: Subdomain Configurations: (Left) Spectral-Spectral-Spectral-WENO. (Middle) Spectral-Spectral-WENO-WENO. (Right) Spectral-WENO-WENO-WENO.

The "Ghost Zones" $G_2^{\mathbf{k}}, G_7^{\mathbf{k}}$ and $G_8^{\mathbf{k}}$ of the WENO subdomain lie in the three neighboring spectral subdomains as shown in Figure 6. The "Ghost Area" points of WENO subdomains are computed via spectral interpolations. To be more specific, referring to the middle figure of Figure 7, the solution in the area of the intersection of S^3 (subdomain $\mathbf{k}$) and W^4 (subdomain $\mathbf{k}_5$) corresponding to the "Ghost Zone" $G_1^{\mathbf{k}}$ in (4.1) (see also Figure 3) is read using the interpolating

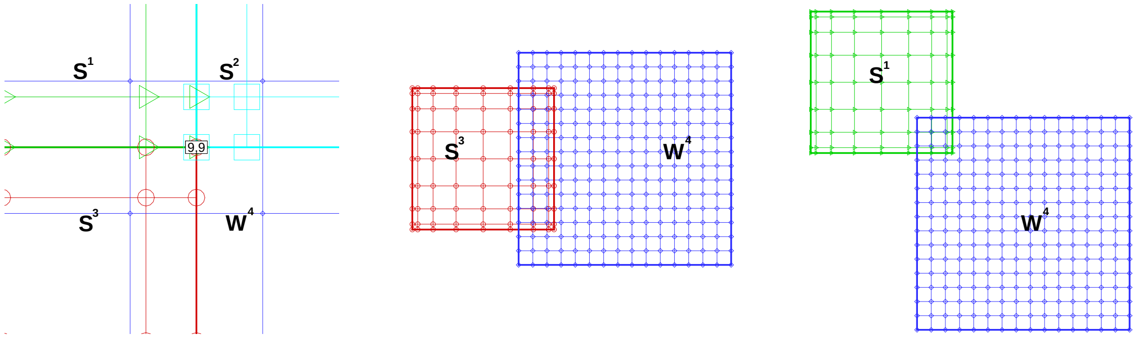

Figure 7: (Left) Spectral-Spectral-Spectral-WENO subdomain configuration. (Middle) $S^3 - W^4$ Interface. (Right) $S^1 - W^4$ Interface.

polynomial representing the solution in S^3, that is, at the subdomain $\mathbf{k}$,

$$w(x_n, y_m) = \sum_{j=0}^{N_S} \sum_{i=0}^{N_S} s_{ij} l_i(x_n) l_j(y_m), \quad m = 0, \ldots, N_W, \quad n = -r, \ldots, -1, \quad (x_n, y_m) \in \mathbf{k}_5 \quad , \tag{4.7}$$

where s_{ij} are the functional values in S^3 (subdomain $\mathbf{k}$), $l_i(x)$ and $l_j(y)$ are Lagrangian interpolation polynomials of degree N_S. The ghost points for the other two configurations can be obtained in a similar way.

The interface points of the spectral subdomain are computed via a two dimensional interpolation polynomial of degree $r = n_W$. The choice of stencils $\{(x_i, y_j), i = -i_0 - r/2, \ldots, i_0 + r/2, j = j_0 - r/2, \ldots, j_0 + r/2\}$ for the interpolation polynomial should be as symmetric about a given point (x_{i_0}, y_{j_0}) as possible.

4.3 The Switching Algorithm

In this section we describe the algorithm used to switch the subdomains spatial discretizations as indicated by the Multi-Resolution Analysis of Section 3. The following three conditions are the main rules to be followed:

1. If a subdomain contains high gradients, then switch its spatial discretization to (or keep it with) WENO;
2. If high gradients are present in the ”Buffer Areas” of connected neighboring subdomains, then switch the current subdomain to (or keep it as) a WENO subdomain;
3. In any other case, switch the subdomain to (or keep it as) a spectral subdomain;

The first condition above avoids the Gibbs phenomenon, keeping the discontinuities inside WENO subdomains. The second condition ensures the switch to WENO subdomain in order to allow only WENO-to-WENO transmission of discontinuities. The third condition improves the numerical efficiency, since it ensures that smooth parts of the solution will always be contained in spectral subdomains.

Multi-Resolution analysis of the solution is performed at every sub-stage of the third order TVD Runge-Kutta scheme used for the temporal evolution. At each subdomain **k**, we define the smoothness flag variable, $\mathrm{Flag}_{ij}^{\mathbf{k}}$, at each grid point (x_i, y_j) including the ghost points, as ,

$$\mathrm{Flag}_{ij}^{\mathbf{k}} = \begin{cases} 1, & |d_{ij}^{\mathbf{k}}| > \epsilon_{MR} \quad \text{for} \quad (x_i, y_j) \subseteq I^{\mathbf{k}} \bigoplus B_l^{\mathbf{k}} \quad l = \mathbf{A}, \dots, \mathbf{H} \\ 0, & \text{otherwise} \end{cases} . \tag{4.8}$$

where $d_{ij}^{\mathbf{k}}$ are the MR coefficients. Since the Multi-Resolution Analysis requires uniformly spaced grids, the spectral grids are first interpolated to uniformly spaced grids before obtaining the MR coefficients $d_{ij}^{\mathbf{k}}$. The necessary ghost points are acquired from the neighboring subdomains. At the boundary subdomains, the value of the boundary ghost points are extrapolated linearly from the interior data.

The algorithm proceeds by checking for each subdomain **k** and at the buffer zones of the neighboring subdomains if $\mathrm{Flag}_{ij}^{\mathbf{k}}$ is equal to one. If so, it switches subdomain **k** to a WENO discretization. On the other hand, if $\mathrm{Flag}_{ij}^{\mathbf{k}}$ is identically zero, then a spectral discretization is implemented, or kept. These switches require the use of interpolation from a Chebyshev grid of points to a uniformly spaced one and vice-versa:

- To switch from the spectral subdomain to the WENO subdomain, the data are interpolated onto the uniformly spaced grid via the spectral interpolation formula.

- To switch from the WENO subdomain to the spectral subdomain, the data are interpolated onto the Chebyshev Gauss-Lobatto points via the Lagrangian interpolation polynomial of the same order as the WENO method.

Remark 4.1. Back and forth switching between WENO and spectral discretizations may occur too frequently for the same domain when the ϵ_{MR} is marginally set. The $d_{ij}^{\mathbf{k}}$ coefficients might oscillate around the parameter ϵ_{MR} in time due to some numerical factors such as dissipation, dispersion and nonlinear effects, or any combination of such. This pattern of switching can repeat itself for a while until the solution settles down with a clear definition of the $d_{ij}^{\mathbf{k}}$, which is either greater than or smaller than the MR tolerance ϵ_{MR}. In order to alleviate such occurrences, one must devise a procedure preventing the switch from WENO to spectral if it had already occurred recently. However, the procedure must never prevent a spectral to WENO switch, for oscillations and instability might occur.

5 Numerical Results

In this section, we apply the hybrid method to two well-known problems in Conservation Laws: The Shock-Vortex Interaction and the Richtmyer-Meshkov Instability. The governing equations are the two-dimensional Euler equations in Cartesian coordinates given by:

$$\mathbf{Q}_t + \mathbf{F}_x + \mathbf{G}_y = 0 \quad , \tag{5.1}$$

where

$$\begin{aligned}\mathbf{Q} &= (\rho, \rho u, \rho v, E)^T \quad , \\ \mathbf{F} &= (\rho u, \rho u^2 + P, \rho u v, (E+P)u)^T \quad , \\ \mathbf{G} &= (\rho v, \rho u v, \rho v^2 + P, (E+P)v)^T \quad ,\end{aligned} \tag{5.2}$$

and the Equation of state

$$P = (\gamma - 1)(E + \frac{1}{2}\rho(u^2 + v^2)), \qquad \gamma = 1.4. \tag{5.3}$$

We will restrict the following study to rectangular domains, which will be partitioned into an equal number of subdomains in both x and y directions. The number of Chebyshev collocation points for all spectral subdomains will be the same in both x and y directions, as well as the number of uniformly spaced grid points for the WENO subdomains. The order of the Multi-Resolution Analysis is the same as the WENO scheme, $n_{MR} = n_W$. A 14_th order Exponential filter and Kosloff-Tal-Ezer mapping are employed in all spectral subdomains. Free stream boundary conditions are imposed in the inflow and outflow in the x direction and periodical boundary condition is imposed in the y direction. To evolve the ODE from the semi-discretized PDE in time, the third order Total Variation Diminishing Runge-Kutta scheme (RK-TVD) will be used [3]:

$$\begin{aligned}\vec{U}^1 &= \vec{U}^n + \Delta t L(\vec{U})^n \\ \vec{U}^2 &= \frac{1}{4}\left(3\vec{U}^n + \vec{U}^1 + \Delta t L(\vec{U}^1)\right) \quad , \\ \vec{U}^{n+1} &= \frac{1}{3}\left(\vec{U}^n + 2\vec{U}^2 + 2\Delta t L(\vec{U}^2)\right)\end{aligned} \tag{5.4}$$

where L is the spatial operator. The CFL numbers for the spectral and WENO subdomains are set to be 3 and 0.4, respectively. All numerical experiments were run on a 667 MHz Compaq Alpha machine with 1GB memory and with an Alpha internal floating point processor.

5.1 Shock – Vortex Interaction

The tangential velocity profile of the counter-clockwise rotating vortex [17] centered at (x_c, y_c) and strength Γ is given in polar coordinates by:

$$U(r) = \begin{cases} \Gamma r(r_0^{-2} - r_1^{-2}) & 0 \le r \le r_0 < r_1 \\ \Gamma r(r^{-2} - r_1^{-2}) & r_0 \le r \le r_1 \\ 0 & r > r_1 \end{cases} \quad , \tag{5.5}$$

where $r_0 = 0.2$ and $r_1 = 1.0$.

Due to the strong nonlinearity of the shock-vortex interaction its physics are not well understood. A better understanding will have many potential applications, for instance, subsonic and supersonic jet nozzle design and blade noise generation. The Hybrid method will be tested on this problem with a vortex of amplitude $\Gamma = 0.25$ and shock Mach numbers $M_s = 1.25, 3, 6$.

Mach 1.25

In this first example, the physical domain ($0 \leq x \leq 3.9, -2 \leq y \leq 2$) is partitioned into a 13×10 grid of subdomains. Spectral subdomains use a 32×32 grid of Chebyshev points and WENO grids are 50×50. MR analysis is performed with the MR tolerance set to $\epsilon_{MR} = 5 \times 10^{-2}$.

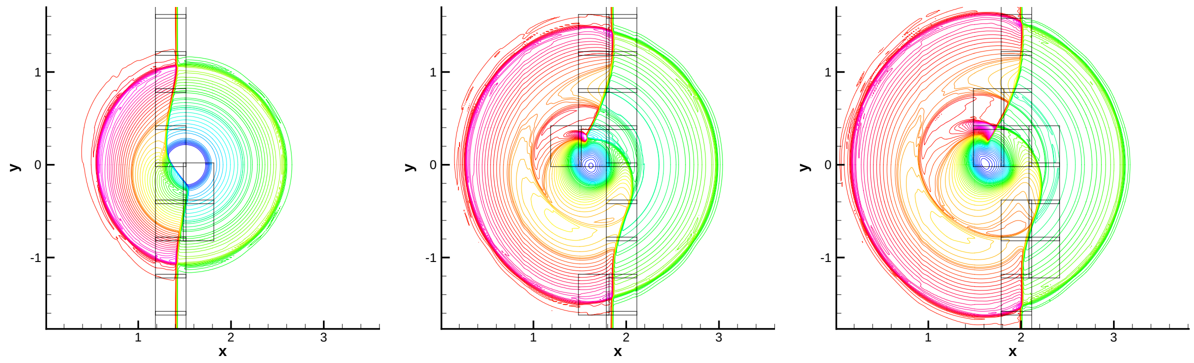

(a) $t = 0.73$ (b) $t = 1.08$ (c) $t = 1.20$

Figure 8: Density ρ of the Shock-Vortex interaction with Mach number $M_s = 1.25$ and $\Gamma = 0.25$ at (a) $t = 0.73$, (b) $t = 1.08$ and (c) $t = 1.2$, as computed by the Hybrid method.

When an initially planar shock wave hits the vortex, it deforms as compression and rarefaction regions are created behind the shock, as shown in Figure 8 for $t = 0.732, 1.08, 1.2$. As the interaction proceeds over time, strong bifurcation and deformation of the shock are observed. The shock emanating from the compression region has one part moving upward and another moving downward. The strength of the lower upward moving part is greater, due to the direction of rotation of the vortex. MR Analysis performed well in capturing the shock and the high gradient regions immediately behind the shock, as indicated by the WENO subdomains enclosed with black bounding boxes. The remaining subdomains are accurately dealt with by the spectral methods. The number of WENO subdomains is far fewer than spectral ones resulting in a more efficient algorithm than the classical WENO scheme.

Mach 3

We now increase the Mach number of the shock from $M_s = 1.25$ to $M_s = 3$ and compare the solution of the Hybrid scheme with a highly resolved one computed with the classical fifth order WENO scheme using 1200×1200 points. The physical domain ($0 \leq x \leq 3.0, -2 \leq y \leq 2$) is partitioned into a 10×10 grid of subdomains and all other parameters are as in Example 1.

As in the previous example, an acoustic wavefront is generated and a number of fine scale structures are formed behind the main shock. This example indicates that the Hybrid method captures the fine features of the solution even in the case of strong shocks.

Mach 6

In this last example, we further increase the shock Mach number to $M_s = 6$ and use a 19×20 grid of subdomains to partition the physical domain $(0 \leq x \leq 4.2, -3 \leq y \leq 3)$. The spectral grid is 16×16. This example shows that the Hybrid method can be applied to higher Mach number flows as well, still resulting on a reliable and efficient shock-capturing method.

5.2 Two-dimensional Richtmyer-Meshkov Instability

Richtmyer in 1960 [22] theoretically predicted the occurrence of instability on a perturbed material interface under the impulsive acceleration of an incident shock wave. In 1970 Meshkov [20] experimentally confirmed these predictions. A variety of motions can be generated following the interaction of a shock wave with an interface separating two materials. Any small perturbation present on the interface will be amplified after such a contact. This class of problems is referred in the literature as the "Richtmyer-Meshkov Instability (RMI)". As the interface between two materials becomes increasingly distorted other instabilities such as the Kelvin-Helmholtz Instabilities develop and a region of turbulence mixing ultimately results. The RMI arises in many applications as, for instance, the Inertial Confinement Fusion (ICF) process. A recent model under extensive study consists of a set of laser beams directed into a chamber containing a spherical fusion fuel target. The expected result should be compression, ignition and a subsequent energy surplus. However, since no perfect capsule exists, irregularities on the surface excite the undesirable RMI, reducing the effective uniform compression pressure onto the capsule.

Presently, a rectangular domain with a shock Mach number M_s interacting with a single mode sinusoidal perturbation along a Xenon (Xe) and Argon (Ar) gases interface is simulated using the Hybrid method. The initial condition is given in Figure 11 and a diffusive interface is modeled with an exponential function, i.e.

$$S(x,y) = \begin{cases} 1 & d \leq 0 \\ \exp(-\alpha |d|^{\beta}) & 0 < d < 1 \\ 0 & d \geq 1 \end{cases} , \tag{5.6}$$

where

$$d = \frac{(x_s + a\cos(2\pi y/\lambda) + \delta) - x}{2\delta}, \tag{5.7}$$

$\delta = 0.2$ cm > 0 is the interface thickness, $\beta = 8$ is the interface order, $x_s = 0.5$ cm is the location of the interface and $\alpha = -\ln\epsilon$, where ϵ is the machine zero. The conservative or primitive variables are scaled according to the $S(x,y)$ between the Xenon and Argon gases.

Mach 4.46

In this example, the physical domain $(0 \leq x \leq 5.1, 0 \leq y \leq \lambda)$ is partitioned into a 17×12 grid of subdomains. The spectral grids are 32×32 and the WENO grids are 50×50. The MR tolerance is now lowered to $\epsilon_{MR} = 5 \times 10^{-5}$.

As the shock wave collides with the interface separating the two gases, the sine wave perturbation is accelerated, compressed and amplified following the refraction of the shock (see Figure 13).

The heavier Xenon gas (Xe) will penetrate into the lighter Argon gas (Ar) forming finger-like structures – bubbles and spikes. A bubble (spike) is a portion of the light (heavy) gas penetrating into the heavy (light) gas. The basic mechanism of these instabilities is the baroclinic generation of vorticity $\vec{\omega}$ induced from the misalignment of the pressure gradient ∇p of the shock and the local density gradient $\nabla \rho$ across the interface:

$$\frac{\partial \vec{\omega}}{\partial t} \sim \nabla p \times \nabla \rho, \qquad \vec{\omega} = \nabla \times \vec{u}, \tag{5.8}$$

where $\vec{u}$ is the velocity. Once again, as seen in Figure 13, the WENO method is activated only along the material interface and where high gradients appear.

Mach 8

The physical domain $(0 \le x \le 24.6, 0 \le y \le \lambda)$ is partitioned into a 82×12 grid of subdomains in order to apply the Hybrid method for a longer time integration up to $t = 100\mu s$. The shock Mach number is increased from $M_s = 4.46$ to $M_s = 8$ and the spectral grid is set to 24×24.

It can be observed in Figure 14 that the Hybrid method successfully tracks shocks and high gradients with WENO discretization (black bounding boxes) while the smooth parts of the solution are well represented using spectral subdomains.

5.3 CPU Timing

The Hybrid method has the potential advantage of being faster than the classical WENO method due to the higher numerical efficiency of spectral methods at smooth parts of the solution. Moreover, spectral discretizations avoid the expensive characteristic decompositions and projections of the WENO method. In this section, we provide some CPU timing results for the Mach 3 Shock-Vortex Interaction (see section 5.1) when using the Hybrid and the classical WENO methods with equal resolution.

The physical domain is partitioned into a set of subdomains of sizes $((10\times 2^j)\times(10\times 2^j)), j = 0, 1, 2, 3$. Spectral subdomains use a 12×12 grid of Chebyshev points and WENO ones use 20×20 grids of uniformly spaced points. The classical fifth-order WENO method, here denoted WENO5, uses the corresponding number of grid points as if all the subdomains in the Hybrid method were WENO subdomains. The MR tolerance used is $\epsilon_{MR} = 5 \times 10^{-2}$.

Table II shows that a significant speed up is achieved when using the Hybrid method over the classical WENO5 for increasing resolution. Figure 15 shows the history of the coverage of the WENO subdomains as a percentage of the total number of the subdomains. This percentage varies between $10\% - 20\%$ for the 10×10 subdomain partition and gets proportionally smaller by a factor of 2 when the number of subdomain partition increases by a factor of 2 in each direction.

Number of subdomains	Grid size	Hybrid S12W20	WENO5	Speedup
10x10	200x200	265	282	1.06
20x20	400x400	2009	2762	1.37
40x40	800x800	14410	26090	1.81
80x80	1600x1600	112900	253996	2.24

Table II: CPU timing in seconds and speedup factor for the Shock-Vortex problem at time $t = 0.6$ as computed by the Hybrid (with constant $\epsilon_{MR} = 5 \times 10^{-2}$) and the WENO5 methods.

Reducing the MR Tolerance level of last experiment to $\epsilon_{MR} = 5 \times 10^{-3}$, while keeping all the other parameters fixed, leads to a slight increase on the CPU time usage for the Hybrid method as compared with the previous case, as shown in Table III. With a lower MR tolerance, more subdomains are classified as containing high gradients.

Number of subdomains	Grid size	Hybrid S12W20	WENO	Speedup
10x10	200x200	332	282	none
20x20	400x400	2239	2762	1.23
40x40	800x800	15580	26090	1.67

Table III: CPU timing in seconds and speedup factor for the Shock-Vortex problem at time $t = 0.6$ as computed by the Hybrid (constant $\epsilon_{MR} = 5 \times 10^{-3}$) and WENO5 methods.

6 Conclusions

We have presented the two dimensional version of the multi-domain Hybrid Spectral-WENO method for nonlinear hyperbolic conservation laws. The rectangular physical domain was partitioned into a grid of subdomains which are either a Chebyshev collocation grid for the spectral method or an uniformly spaced grid for the WENO method. High order Multi-Resolution Analysis is used to measure the smoothness of the solution in a given subdomain and a strategy for switching the subdomain from spectral to WENO when the solution becomes non-smooth and vice versa was devised. The Hybrid method was tested with the shock-vortex interaction and the Richtmyer-Meshkov instability (RMI) two dimensional problems. The results were in good agreement with the classical fifth order WENO finite difference method. In these two cases tested, the switching procedure devised performs well and the coverage of the WENO method were less than 20% of the total number of subdomains resulting in a good speedup and efficient method for shocked flow.

Currently, we are investigating in depth the role of the Multi-Resolution Tolerance ϵ_{MR} and its effects on the Hybrid solution. Furthermore, the implementation of the smoothness measurement in the spectral subdomains can be improved and is also under investigation. Since the Hybrid method is built in a multi-domain framework, parallelization of the method is fairly straightforward; the only required communications between the subdomains are through a small number of ghost points used in the WENO and Multi-Resolution Analysis. A substantial speedup can be achieved with a reasonable and balanced distribution of subdomains to each processor.

We plan to extend the Hybrid method to nonlinear hyperbolic conservation laws systems in three dimensions and with fifth and higher order WENO finite difference methods. One application under consideration is to study the three dimensional reactive flow over a open cavity that serves as the flameholder in a scramjet engine. We also plan to use the Hybrid method for shocked flow over obstacles and other applications with more complex geometries. Non-conforming subdomains with various sizes will be investigated in this future work.

7 Acknowledgments

The author (Costa) has been supported by CNPq, grant 300315/98-8. The authors (Don, Gottlieb and Sendersky) gratefully acknowledge the support of this work by the DOE under contract number DE-FG02-98ER25346 and the AFOSR under contract number FA9550-05-1-0123. Part of the research was performed while the second author (Don) was visiting the Department of Mathematics of the Hong Kong Baptist University and would like to express an appreciation to Prof. Tao Tang for his hospitality.

References

[1] J. P. Boris and D. L. Book. Flux Corrected Transport I, SHASTA, a Fluid Algorithm that Works. *J. Comput. Phys*, 11:38–69, 1973.

[2] C. Canuto, A. Quarteroni, M.Y. Hussaini, and T. Zang. *Spectral Methods in Fluid Mechanics*. Springer-Verlag, New York, 1988.

[3] B. Cockburn, C. Johnson, C.-W. Shu, and E. Tadmor. *Advanced Numerical Approximation of Nonlinear Hyperbolic Equations*, volume 1697 of *Lecture Notes in Mathematics*, chapter Essentially Non-Oscillatory and Weighted Essentially Non-Oscillatory Schemes for Hyperbolic Conservation Laws, pages 325–432. Springer, Cetraro, Italy, 1997. Editor: A. Quarteroni.

[4] B. Costa and W.-S. Don. On the Computation of High Order PseudoSpectral Derivatives. *Applied Numerical Mathematics*, 33:151–159, 2000.

[5] W.-S. Don. Numerical Study of PseudoSpectral Methods in Shock Wave Applications. *J. Comput. Phys.*, 110(1):103–111, 1994.

[6] W.-S. Don and B. Costa. Multi-Domain Hybrid Spectral-WENO Methods for Conservation Laws. In preparation.

[7] W.-S. Don and A. Solomonoff. Accuracy and Speed in Computing the Chebyshev Collocation Derivative. *SIAM, J. Sci. Comput.*, 16(6):1253–1268, November 1995.

[8] W.-S. Don and A. Solomonoff. Accuracy Enhancement for Higher Derivatives using Chebyshev Collocation and a Mapping Technique. *SIAM, J. Sci. Comput.*, 18(4):1044–1055, July 1997.

[9] D. Gottlieb, L. Lustman, and C. S. Streett. *Spectral Methods for Partial Differential Equations*, chapter Spectral Methods for Two Dimensional Shocks, page 79. SIAM-CBMS. Society for Industrial and Applied Mathematics, Philadelphia, 1984. Edited by R.G. Voigt and D.Gottlieb and M.Y. Hussaini.

[10] D. Gottlieb and S. Orszag. *Numerical Analysis of Spectral Methods: Theory and Applications*. Society for Industrial and Applied Mathematics, Philadelphia, 1977.

[11] D. Gottlieb, C.-W. Shu, A. Solomonoff, and H. Vandeven. On the Gibbs Phenomenon I: Recovering Exponential Accuracy from the Fourier Partial Sum of a Nonperiodic Analytic Function. *J. Comput. Appl. Math*, 43:81–92, 1992.

[12] A. Harten. High Resolution Schemes for Hyperbolic Conservation Laws. *J. Comput. Phys.*, 49:357–393, 1983.

[13] A. Harten. Adaptive Multiresolution Schemes for Shock Computations. *J. Comput. Phys.*, 115:319–338, 1994.

[14] A. Harten, B. Engquist, S. Osher, and S. Chakravarthy. Uniformly High-Order Accurate Essentially Non-Oscillatory Schemes III. *J. Comput. Phys.*, 71:231–303, 1987.

[15] G. Jiang and C.-W. Shu. Efficient Implementation of Weighted ENO Schemes. *J. Comput. Phys.*, 126:202–228, 1996.

[16] J.-H. Jung and B. D. Shizgal. Generalization of the Inverse Polynomial Reconstruction Method in the Resolution of the Gibbs Phenomenon. *J. Comput. Applied Math.*, 172(1):131–151, 2004.

[17] D. A. Kopriva. A Multidomain Spectral Collocation Computation of the Sound Generated by a Shock-Vortex Interaction. *Computational Acoustics: Algorithms and applications*, 2, 1988. D. Lee and M. H. Schultz (eds.).

[18] D. Kosloff and H. Tal-Ezer. Modified Chebyshev PseudoSpectral Methods with $O(N^{-1})$ Time Step Restriction. *J. Comput. Phys.*, 104:457–469, 1993.

[19] X.-D. Liu, S. Osher, and T. Chan. Weighted Essentially Non-Oscillatory Schemes. *J. Comput. Phys.*, 115:200–212, 1994.

[20] E. E. Meshkov. Instability of a Shock Wave Accelerated Interface between Two Gases. *NASA*, F-13:074, 1970.

[21] M.-S. Min, M. S. Kaber, and W.-S. Don. Fourier-Padé Approximations and Filtering for the Spectral Simulations of Incompressible Boussinesq Convection Problem. *Publications du Laboratorie Jacques-Louis Lions, R03021, Mathematics of Computation*, 2004.

[22] R. D. Richtmyer. Taylor Instability in Shock Acceleration of Compressible Fluids. *Comm. Pure Appl. Math*, 13:297–319, 1960.

[23] P. L. Roe. Approximate Riemann Solvers, Parameter Vectors, and Difference Schemes. *J. Comput. Phys.*, 43:357–372, 1981.

[24] K. Sebastian. *Multi Domain Weighted Essentially Non Oscillatory (WENO) Method With Interpolation at Subdomain Interfaces.* PhD thesis, Brown University, May 2003.

[25] B. van Leer. Towards the Ultimate Conservative Difference Scheme. A Second Order Sequel of Godunov's Method. *J. Comput. Phys.*, 32:101–136, 1979.

[26] H. Vandeven. Family of Spectral Filters for Discontinuous Problems. *J. Sci. Comput.*, 8:159–192, 1991.

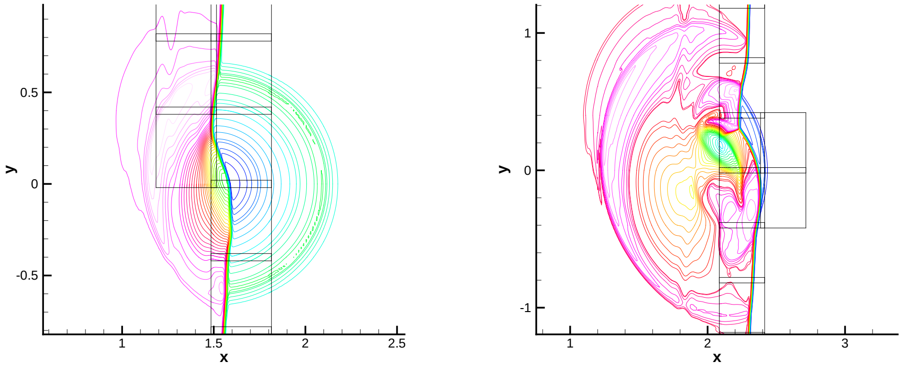

(a) $t = 0.35$, Hybrid Scheme (b) $t = 0.60$, Hybrid Scheme

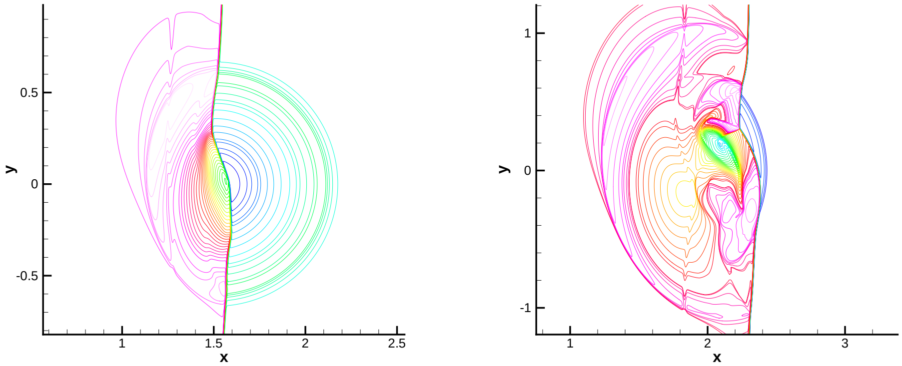

(c) $t = 0.35$, WENO5 Scheme (d) $t = 0.60$, WENO5 Scheme

Figure 9: Density ρ of the Shock-Vortex interaction with Mach number $M_s = 3$ and $\Gamma = 0.25$ at time (a) $t = 0.35$ and (b) $t = 0.6$ as computed by the Hybrid scheme and (c) $t = 0.35$ and (d) $t = 0.6$ as computed by the classical fifth order WENO finite difference scheme (WENO5) with 1200×1200 grid points.

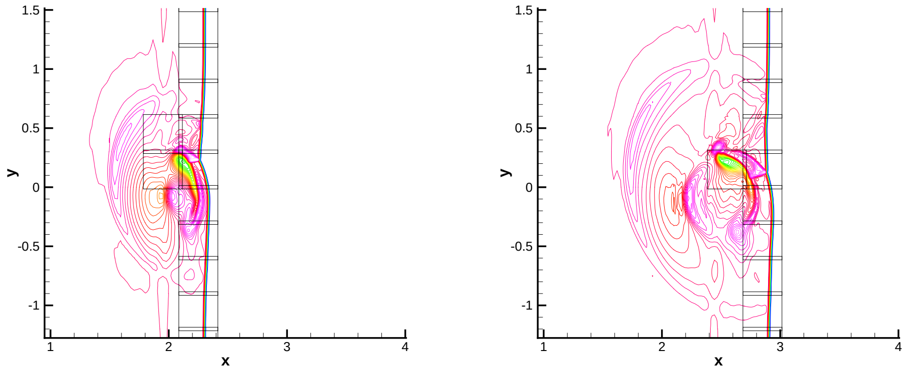

(a) $t = 0.3$

(b) $t = 0.4$

Figure 10: Density ρ of the Shock-Vortex interaction with Mach number $M_s = 6$ and $\Gamma = 0.25$ at time (a) $t = 0.3$ and (b) $t = 0.4$ as computed by the Hybrid method.

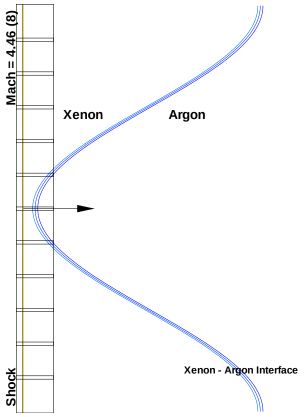

1) Rankine-Hugoniot condition for shocks
2) Pre-Shock Temperature $T = 296$ K
3) Pre-Shock Pressure $P = 0.5$ atm
4) Xenon density $\rho_{Xe} = 2.90 \times 10^{-3}\ \frac{\mathrm{g}}{\mathrm{cm}^3}$
5) Argon density $\rho_{Ar} = 0.89 \times 10^{-3}\ \frac{\mathrm{g}}{\mathrm{cm}^3}$
6) Specific heat ratio $\gamma = \frac{5}{3}$
7) Atwood number $At = 0.54$
8) Mach number $M = 4.46$
9) Wave Length $\lambda = 3.6$ cm
10) Amplitude $a = 1.0$ cm

Figure 11: Initial Condition for the Richtmyer-Meshkov Instability simulation.

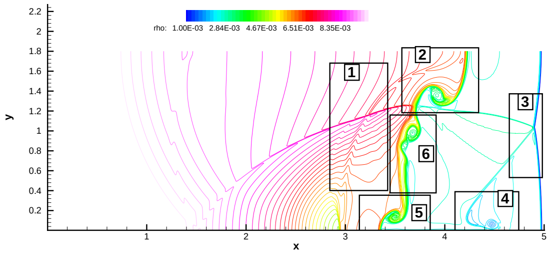

Regions of Interest :

1) Reflected shock generated by the shock refraction;
2) The penetration of the heavy (Xe) to light (Ar) gas forms the Spike;
3) Triple point on the transmitted shock;
4) A small jet and its vortical structure;
5) The penetration of the light (Ar) to heavy (Xe) gas forms the Bubble;
6) Vortical rollups of the gaseous interface.

Figure 12: Typical regions of interest for the simulation of the RMI at time $t = 50\,\mu s$. Only the lower half of the interface is shown.

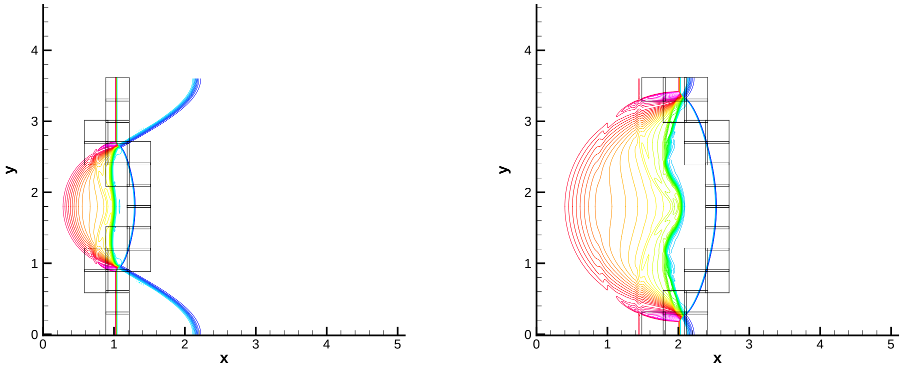

(a) $t = 12.5\,\mu s$ (b) $t = 25.0\,\mu s$

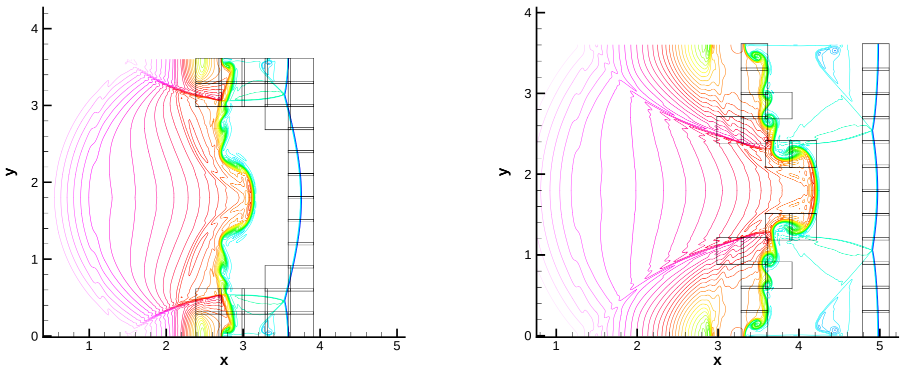

(c) $t = 37.5\,\mu s$ (d) $t = 50.0\,\mu s$

Figure 13: Contour plot of the density ρ with $M_s = 4.46, \lambda = 3.6$ cm, $a = 1$ cm at time (a) $t = 12.5\,\mu s$, (b) $t = 25.0\,\mu s$, (c) $t = 37.5\,\mu s$ and (d) $t = 50.0\,\mu s$ of the Richtmyer-Meshkov Instability as computed by the Hybrid scheme.

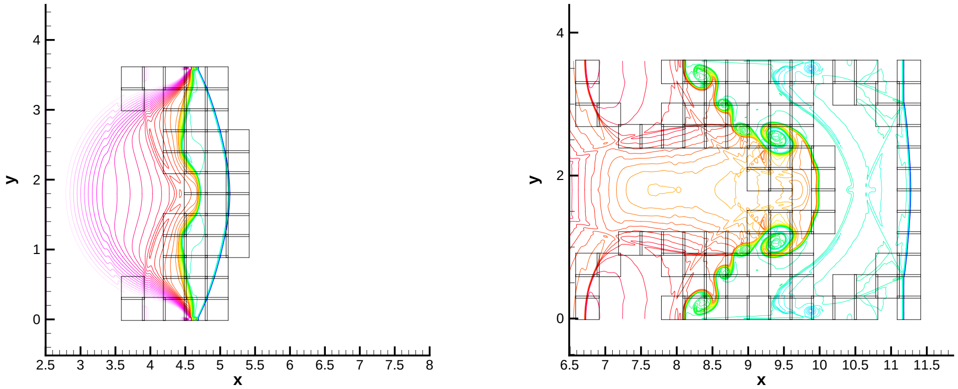

(a) $t = 18.5\,\mu s$ (b) $t = 52.0\,\mu s$

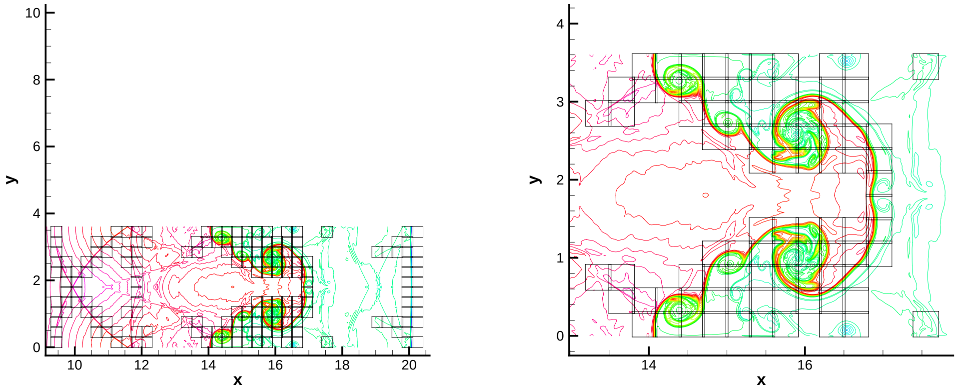

(a) $t = 100.0\,\mu s$ (b) $t = 100.0\,\mu s$ with zoom

Figure 14: Contour plot of the density ρ with $M_s = 8, \lambda = 3.6$ cm, $a = 1$ cm at time (a) $t = 18.5\,\mu s$, (b) $t = 52.0\,\mu s$, (c) $t = 100.0\,\mu s$ and (d) $t = 100.0\,\mu s$ with zoom of the Richtmyer-Meshkov Instability as computed by the Hybrid scheme.

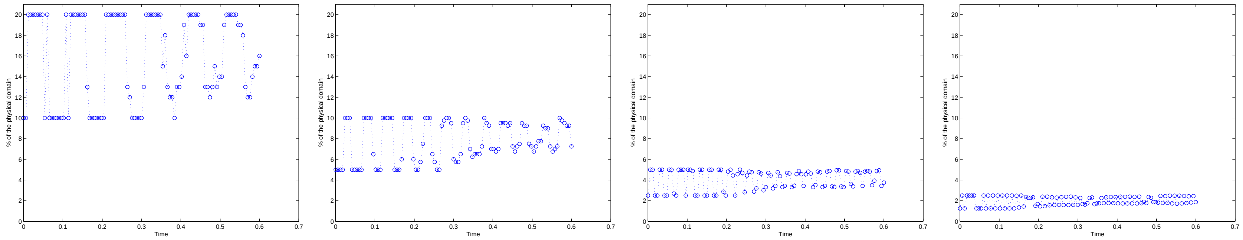

Figure 15: The time history of the coverage of the WENO subdomains as a percentage of total number of subdomains for the four subdomain partitions: (from left to right) $(10\times10), (20\times20), (40\times40), (80\times80)$.